

## 3D Structure of the Skeletal Muscle Dihydropyridine Receptor

Ming-Chuan Wang<sup>1</sup>, Giles Velarde<sup>1</sup>, Robert C. Ford<sup>1</sup>  
Nicholas S. Berrow<sup>2</sup>, Annette C. Dolphin<sup>2</sup> and Ashraf Kitmitto<sup>1\*</sup>

<sup>1</sup>Department of Biomolecular Sciences, University of Manchester Institute of Science and Technology (UMIST) P.O. Box 88, Manchester M60 1QD, UK

<sup>2</sup>Department of Pharmacology University College London Gower Street, London, WC1E 6BT, UK

The dihydropyridine receptors (DHPR) are L-type voltage-gated calcium channels that regulate the flux of calcium ions across the cell membrane. Here we present the three-dimensional (3D) structure at  $\sim 27$  Å resolution of purified skeletal muscle DHPR, as determined by electron microscopy and single particle analysis. Here both biochemical and 3D structural data indicate that DHPR is dimeric. DHPR dimers are composed of two arch-shaped monomers  $\sim 210$  Å across and  $\sim 75$  Å thick, that interact very tightly at each end of the arch. The roughly toroidal structure of the two monomers encloses a cylindrical space of  $\sim 80$  Å diameter, which is then closed on each side by two dome-shaped protein densities reaching over from each monomer arch. The dome-shaped domains have a length of  $\sim 80$ – $90$  Å and a maximum height of  $\sim 45$  Å. Small orifices punctuate their exterior surface. The 3D structure disclosed here may have important implications for the understanding of DHPR  $\text{Ca}^{2+}$  channel function. We also propose a model for its *in vivo* interactions with the calcium release channel at the junctional sarcoplasmic reticulum.

© 2002 Elsevier Science Ltd. All rights reserved

**Keywords:** dihydropyridine receptor; electron microscopy; L-type voltage-gated calcium; 3D reconstruction; negative staining

\*Corresponding author

### Introduction

L-type voltage-gated calcium channels (VGCC) mediate the flux of calcium ions across cell membranes, in response to changes in membrane potential. In excitable cells such as neurons, heart and skeletal muscle membranes, VGCC are responsible for coupling membrane potential changes to biological functions such as secretion, neurotransmitter release, and muscle contraction.<sup>1</sup> One group of drugs binding to these calcium channels with nanomolar binding constants are the dihydropyridines,<sup>2</sup> and thus L-type VGCC are also commonly referred to as dihydropyridine receptors (DHPR); the nomenclature we will use here. In

addition to functioning as calcium channels the DHPRs serve, in skeletal muscle, as voltage sensors for initiation of muscle excitation–contraction (E–C) coupling.<sup>3</sup> However, as yet the exact mechanism of muscle E–C coupling at the molecular level is not fully understood.<sup>4,5</sup>

Purification of the skeletal muscle DHPR by a number of groups<sup>6–8</sup> determined that these ion channels are hetero-oligomeric membrane protein complexes, composed of at least four non-covalently associated polypeptides, encoded by four separate genes:<sup>9</sup>  $\alpha 1$  ( $\sim 170$  kDa),  $\alpha 2\delta$  ( $\sim 170$  kDa),  $\beta$  ( $\sim 55$  kDa), and  $\gamma$  ( $\sim 30$  kDa). The subunit forming the ion channel pore, and responsible for the influx of  $\text{Ca}^{2+}$  across the lipid bilayer is the  $\alpha 1$  polypeptide. Topological analysis of the  $\alpha 1$  subunit amino acid sequence, reveals a phylogenetically conserved motif found in a variety of different cation channels such as the voltage-gated sodium and potassium channels.<sup>10</sup> Sequence analysis of the  $\alpha 1$  polypeptide predicts 24  $\alpha$ -helical transmembrane segments arranged as four repeats.<sup>11</sup> The  $\alpha 2\delta$  subunit is composed of two proteins  $\alpha 2$  ( $\sim 143$  kDa) and  $\delta$  ( $\sim 25$ – $17$  kDa) linked *via* disulphide bonds.<sup>12,13</sup> The  $\delta$  peptide, containing a single transmembrane segment,<sup>14</sup> is thought to anchor

Present address: G. Velarde, School of Biological Sciences, University of Manchester, Stopford Building, Oxford Road, Manchester, M13 9PT, UK.

Abbreviations used: DHPR, dihydropyridine receptor; EM, electron microscopy; Chaps, (3-[(cholamidopropyl)-dimethyl-ammonio]-1-propanesulphonate); WGA, wheat germ agglutinin; 2D, two-dimensional; 3D, three-dimensional; FSC, Fourier shell correlation; DPR, differential phase residual; RyR, ryanodine receptor.

E-mail address of the corresponding author: a.kitmitto@umist.ac.uk

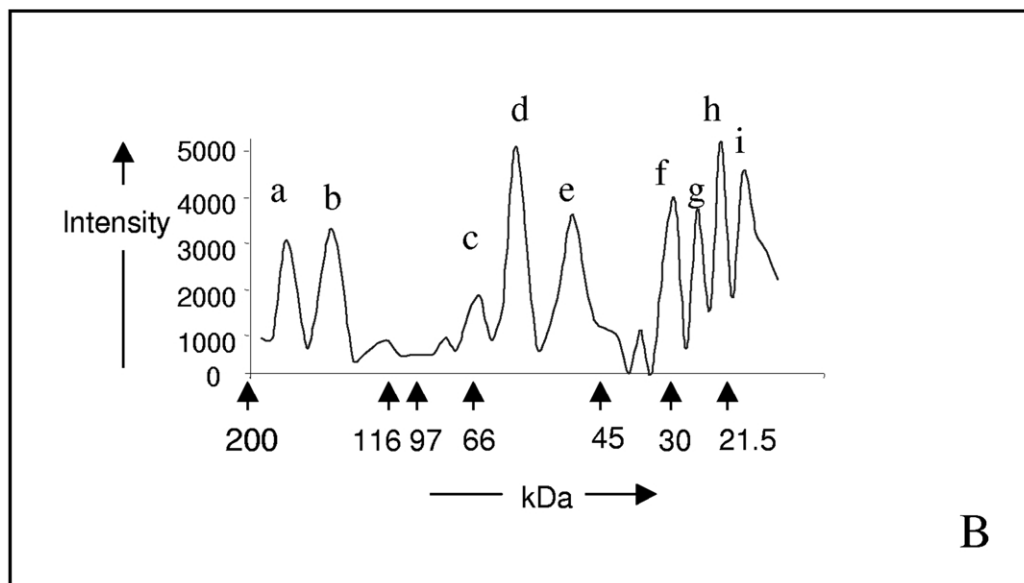
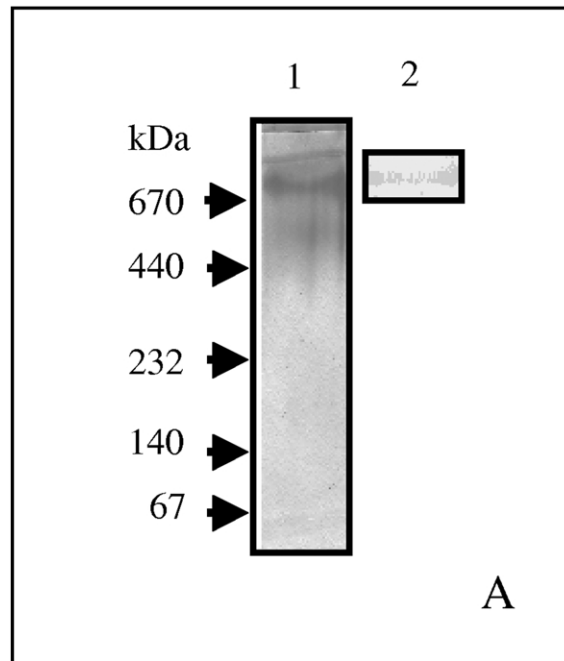


**Figure 1.** Characterisation of an oligomeric DHPR complex. (a) Lane 1, Native gel of purified DHPR showing a silver-stained protein band at  $\sim 750$  kDa; lane 2, immunoblot (anti-beta antibody) of the native gel showing labelling of the  $\sim 750$  kDa band. (b) Densitometric scan of DHPR polypeptides after the denaturation of the  $\sim 750$  kDa protein complex and SDS-PAGE.

the highly glycosylated extracellular  $\alpha 2$  protein to the lipid bilayer.<sup>15,16</sup> Hydropathy plots indicate that the intracellular  $\beta$  subunit is a hydrophilic polypeptide,<sup>17</sup> whereas the primary sequence of the  $\gamma$  subunit suggests it is composed of four putative transmembrane segments.<sup>15</sup> The functions of these auxiliary polypeptides ( $\alpha 2\delta$ ,  $\beta$  and  $\gamma$ ) are less clear, though roles in membrane targeting, stabilisation and channel gating have been reported by a large number of groups.<sup>15,19–23</sup>

The DHPRs have been extensively studied in terms of electrophysiological and pharmacological properties, however there is a paucity of data pertaining to structure. This has been probably due in part to the low natural abundance of the ion channel in most tissue types, and difficulties in isolation, purification, and expression. Freeze-fracture images of t-tubular membranes<sup>24,25</sup> showed a tetrad arrangement of the DHPR, i.e. groups of four particles, organised in two rows, that are spatially

orientated to allow superimposition and interdigitation with the calcium release channel, also termed the ryanodine receptor (RyR), which is localised to the junctional sarcoplasmic reticulum (jSR) and bridges the junctional gap. These data provided strong evidence for a muscle E–C coupling model involving a direct interaction of the DHPR and the RyR (see review<sup>26</sup>). Rotary shadowed images of freeze-dried DHPR, purified from solubilised triad junctions,<sup>27</sup> showed particles ovoid in shape, with a central indentation, and with short and long dimensions of approximately 16 nm and 22 nm. Four of these oval complexes were proposed to be required to form the tetrad structures observed in freeze-fracture images.

Single particle image analysis (SPA) is a powerful technique for the structural study of large protein complexes that are not readily amenable to crystallisation.<sup>28–31</sup> The development of image processing techniques designed to analyse non-crystalline large macromolecular complexes such as membrane proteins has allowed the determination of a number of 3D structures<sup>32,33</sup> at medium/low resolutions ( $\sim 30$  Å) with SPA of some viruses sufficient to reveal details of secondary structure.<sup>34</sup> Recently Murata and co-workers<sup>35</sup> presented two dimensional (2D) projection maps of negatively stained purified rabbit skeletal muscle DHPR determined by SPA techniques. Structures at 30 Å resolution, showed a monomeric DHPR complex approximately 200 Å in height and 90 Å in width. The use of negative staining is widespread and it has been successfully employed for studying the size, shape, and oligomeric form of macromolecules<sup>36</sup> as well as for the investigation of subunit–subunit interactions,<sup>37</sup> and large scale conformational changes.<sup>38</sup> Here we have used negative staining coupled with single particle analysis to study large dimeric DHPR complexes with very similar dimensions and gross structural features to those first observed by Leung and co-workers.<sup>27</sup> These dimeric complexes are equivalent to two of the monomeric particles observed by Murata *et al.*<sup>35</sup> We present here a three dimensional (3D) structure for this VGCC.

## Results

### Purification

DHPR was purified using an established protocol.<sup>6–8</sup> Typical yields of purified DHPR were found to range between 90 and 140  $\mu\text{g}/400$  g wet skeletal muscle. DHPR samples were characterised by SDS-PAGE (Figure 1) and by immunoblotting with affinity-purified antibody Ab2491 (reactive with skeletal muscle  $\beta$  subunit from rat and rabbit t-tubule preparations and also with all rat  $\beta$  isoforms 1–4)<sup>39</sup> as well as antisera raised against the  $\alpha 2/\delta$  protein (Ab2079) (an anti-VGCC  $\alpha 2/\delta$  antiserum reactive with skeletal muscle from rat and rabbit t-tubule preparations).<sup>15</sup> Purified DHPR

complexes were also examined by native gel electrophoresis displaying a single high molecular mass band at  $\sim 750$  kDa (Figure 1(a), lane 1). Immunoblotting with anti-beta peptide antibody Ab2491 gave a single band corresponding to the same mass (Figure 1(a), lane 2). The native gel band (750 kDa) was extracted and the recovered protein examined by SDS-PAGE (Figure 1(b) (see Materials and Methods). Due to the varying background intensity from the high to low mass end of the silver-stained broad-range gel the gel was digitised and the background subtracted. The polypeptide composition corresponded to the published literature<sup>6–8</sup> for skeletal muscle DHPR. Two high molecular mass bands at  $\sim 170$  kDa (peak a) and  $\sim 140$  kDa (peak b) correspond to the  $\alpha 1$  and  $\alpha 2$  polypeptides. The lower molecular mass band (e) at  $\sim 55$  kDa is the expected position of the  $\beta$  subunit. A further four bands (denoted f–i) between  $\sim 32$  kDa and 17 kDa were also observed, corresponding to  $\gamma$ ,  $\delta 1$ ,  $\delta 2$  and  $\delta 3$  polypeptides, respectively. The presence of the  $\delta 1$ ,  $\delta 2$  and  $\delta 3$  polypeptides indicates a heterogeneous  $\delta$  subunit population due to variable glycosylation as reported.<sup>14</sup> Peaks (c) and (d) at  $\sim 66$  kDa and  $\sim 60$  kDa, respectively, corresponded to silver stain artefacts and were observed in the absence of protein. The appearance of these two bands has been previously documented.<sup>40</sup> An aliquot of the electroeluted protein from the  $\sim 750$  kDa native gel band was examined by EM, revealing a homogeneous particle population, almost spherical in shape with a diameter of  $\sim 200$  Å (data not shown). These dimensions and overall shape were found to be virtually identical with electron micrographs of the purified DHPR shown in Figure 2.

### Structural analysis of purified DHPR complexes

Presented in Figure 2(a), top panel, is an electron micrograph of the DHPR preparation in negative stain. The particles are homogeneous and uniform in shape, suggesting a favoured orientation of DHPR to the EM grid. Preferred orientations of protein associating with EM grids is a well established phenomenon.<sup>41</sup> Factors influencing this orientation are complex and involve properties of the negative stain, interactions of the protein with the stain and the EM grid support film, charge effects and protein surface topology. Due to the presentation of a preferred view of the DHPR complex the random-conical tilt method<sup>31</sup> was used for the 3D reconstruction. This technique is widely employed for 3D reconstructions of macromolecules,<sup>42</sup> and allows reconstructions to be determined from one orientation of a complex.<sup>43,32</sup>

The micrograph presented in Figure 2(b) represents the same area of the grid after tilting to  $50^\circ$ . 2D alignment and classification of the untilted data set revealed six major classes with estimated spatial resolutions ranging between 25 Å and 35 Å (see Figure 2, bottom panel, row A, and Table 1).

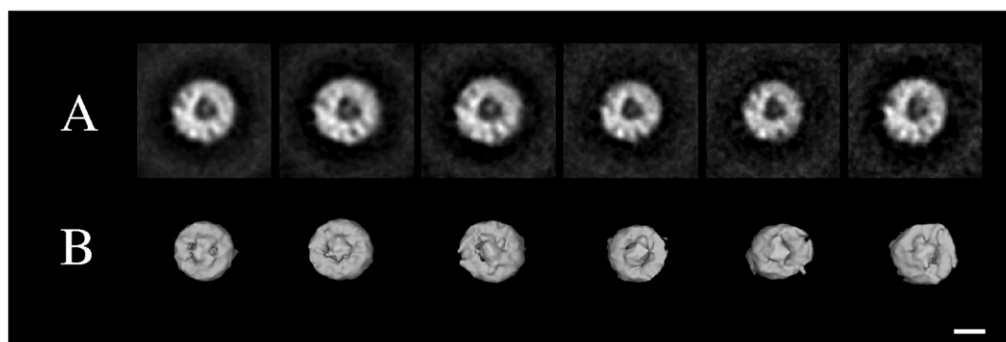
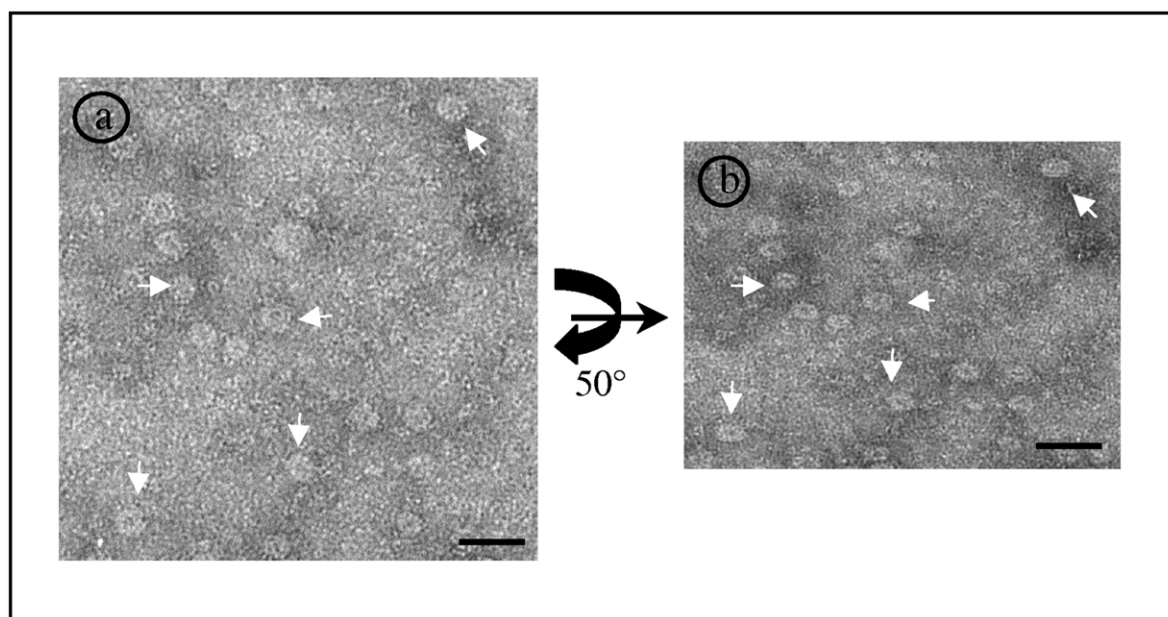


**Figure 2.** Top panel, electron micrographs of purified, negatively stained, DHPR complexes. (a) Untilted micrograph showing particles approximately 20 nm in diameter (arrows). (b) The same area as shown in (a) tilted by 50°. Examples of corresponding particles in each micrograph (tilt pairs) are indicated by arrows. Scale bar represents 50 nm. Bottom panel, row A: 2D projections of the six class averages (untilted dataset). Row B: corresponding 3D volumes (tilted dataset) reconstructed for each class (see Table 1). Scale bar represents 10 nm.

The projections calculated from these six classes appeared to display roughly the same view with slightly different orientations with respect to the EM grid support film and each other (see Table 1). Each 2D average displays an almost circular shape with diameters ranging from 220 Å to 195 Å and distinguished by a large central stain-filled cavity ~50 Å across, though some protein density can be seen in each image to be partially obscuring the cavity. Surface rendered 3D volumes reconstructed (at 1.2 times the standard deviation ( $\sigma$ ) above the mean density) for each of these group averages from the corresponding tilted data, prior to merging, are displayed in row B, bottom panel, Figure 2. Each volume displays a very similar toroidal structure with a smaller protruding density in the centre. Back projections of each of the 3D volumes gave good correlation to the averaged 2D projec-

tion maps in row A (data not shown) as would be expected, since the methodology employed uses the simultaneous iterative reconstruction technique (SIRT) that works to minimise the discrepancy between the two maps. This approach is reported to reduce elongation effects during the reconstruction as a result of the “missing cone”.<sup>44</sup>

A final 3D reconstruction of DHPR at ~27 Å resolution (see Table 1) was generated from 1887 images using standard methodology<sup>31</sup> as described in Materials and Methods. The 3D structure of the purified DHPR is displayed in Figure 3 using mesh of different colours to delineate different density levels. In (a)–(c) of the top panel in Figure 3 yellow and red mesh correspond to density levels of 1.6 and 1.25  $\sigma$  above the mean density, respectively. The pink netting in Figure 3(a) is at 2.6  $\sigma$  above the mean. No symmetry has been applied

**Table 1.** Summary of image processing data

Class average	No. of particles	Resolution (Å)	Euler angles (°) <sup>a</sup>		
			Phi	Theta	Psi
2D projections (Figure 2)					
1	557	26	0	0	0
2	426	27	0.0292	-0.0018	-0.0298
3	304	27	0.1523	-0.0044	-0.1526
4	268	28	-75.8631	5.2138	94.3392
5	192	29	90.3224	-4.7481	-90.3353
6	140	34	-0.2394	-0.0043	0.2396
3D volume (Figure 3)					
No. of particles	1887				
Resolution (Å) (FSC)	25				
Netting colour	x $\sigma$ above mean density	Protein mass <sup>b</sup> enclosed by different thresholding (MDa)			
Pink	2.6	1.40			
Yellow	1.6	0.98			
Red	1.25	0.12			

Upper part of the Table gives data on class averages and the Euler rotation angles applied for merging into the 3D reconstruction. The lower portion relates to the 3D DHPR volume giving the approximate protein mass that could be incorporated in the structure at different thresholds.

<sup>a</sup> Relative to class average 1.

<sup>b</sup> Using  $0.73 \text{ cm}^3 \text{ g}^{-1}$ .<sup>61</sup>

at this stage. The montage begins in Figure 3(a) with a view perpendicular to the grid support film where the structure resembles the projection classes (Figure 2). However, it is clear that the central stained region ( $\sim 85 \text{ Å} \times 85 \text{ Å} \times 85 \text{ Å}$  in size) observed in the particles shown in Figure 2 is not devoid of protein density (arrow). After rotation around the vertical axis by  $45^\circ$  a much clearer impression of the 3D structure becomes apparent (Figure 3(b)). A finger-like protrusion of density (arrow) (yellow and red mesh combination) extends upwards and over the upper surface of the central cavity formed by the main body of protein. Further rotation by  $180^\circ$  around the vertical axis (Figure 3(c)) shows a very similar view of a second finger-like protrusion (yellow mesh only) that is clearly related by 2-fold symmetry to the first. In Figure 3(d) with red mesh corresponding to  $1.25 \sigma$ , and pink to  $2.4 \sigma$  above the mean density, the finger-like protrusions are seen to partially seal the central stain cavity from the exterior, forming a dome-shaped density with a base length of  $\sim 80\text{--}90 \text{ Å}$  and a maximum height of  $\sim 45 \text{ Å}$ . With thresholds used here for display small holes can be seen to punctuate the surface of the finger/dome domains (broken arrow). In Figure 3(d) it can also be seen that the main body of density is split into two arch-shaped densities that are joined at each end of the complex (arrows). The arch-shaped densities are themselves segregated into about four or five lesser domains, which also map onto corresponding domains in the other half of the complex. Thus a C2 axis running through the DHPR complex is readily identified. Figure 3(e) shows a view rotated by  $90^\circ$  with respect to Figure 3(a), i.e. a view parallel with the grid support film

and perpendicular to the C2 axis. Some effects due to differential staining can be noted in this view, with the side labelled B slightly less contrasted than side A. In the 3D reconstruction this side of the particle is the one furthest from the grid support film, agreeing with the usual expectations for stain distribution.<sup>45,46</sup> Figure 3(f) shows the same view of the DHPR dimer after the imposition of 2-fold symmetry on the map. Apart from some smoothing, there is little change to the overall shape of the complex, as would be expected for a homodimeric structure. These results also suggest that the effects of differential staining are relatively minor, and do not have a detrimental effect on the 3D reconstruction.

The resolution of the 3D volume (unsymmetrised) was estimated by the Fourier shell correlation (FSC)<sup>47</sup> and differential phase residual (DPR)<sup>48</sup> techniques. Values of  $25 \text{ Å}$  and  $30 \text{ Å}$  were calculated, respectively, which are in line with expected resolutions from structures determined from negatively stained samples. The true resolution of the volume probably lies midway between the FSC and DPR values, though this will be direction-dependent with the resolution along the z-axis (i.e. perpendicular to the specimen plane) likely to be lower due to the well established missing-cone phenomenon.

The volume of the DHPR complex has been measured at various cut-off density levels for the 3D map (see Table 1). Estimations of the protein mass for the complex will depend on the density level chosen. At intermediate thresholds, as indicated by the yellow mesh, the mass corresponding to this volume could accommodate a DHPR dimer structure.

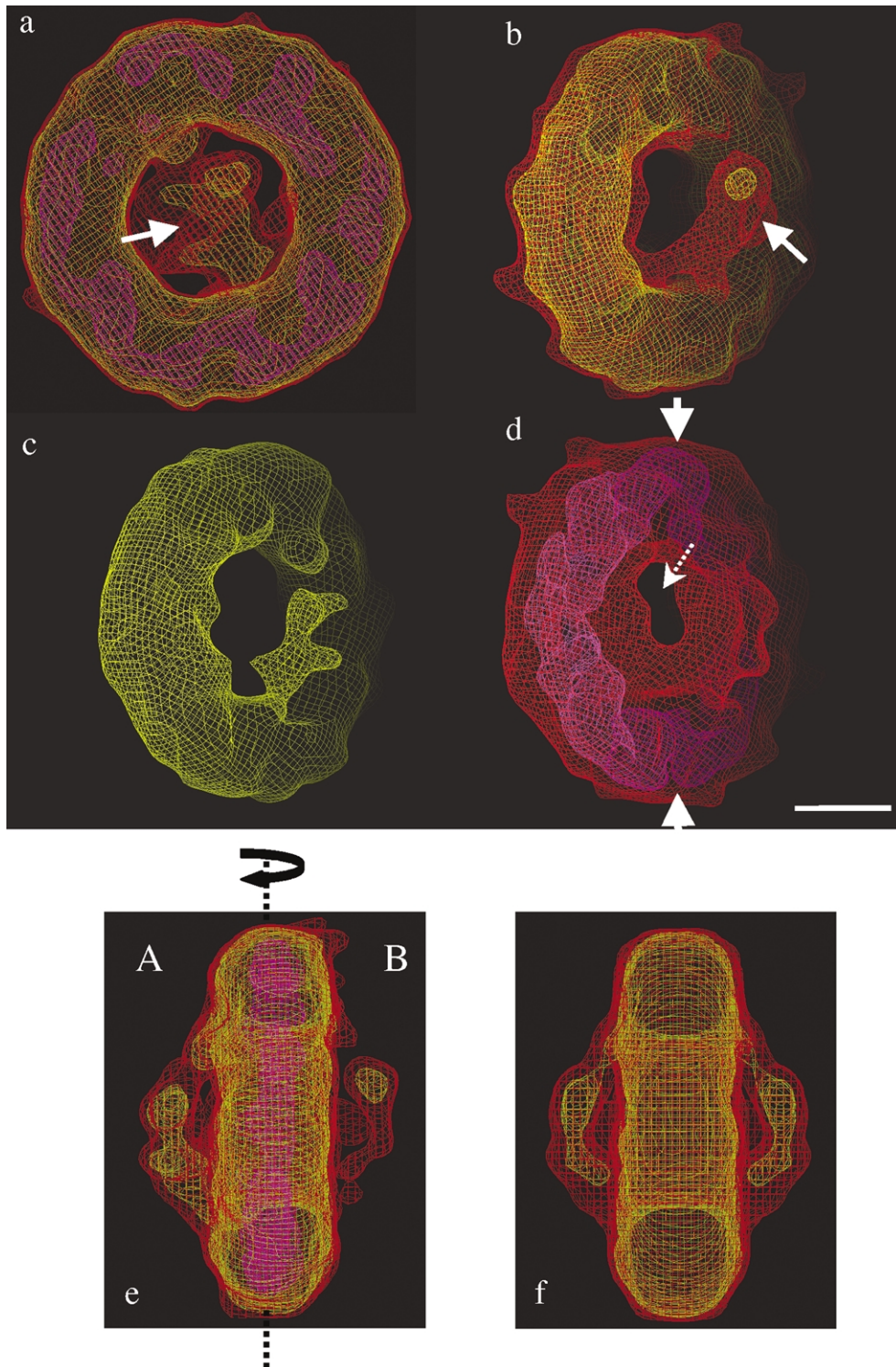


**Figure 3.** 3D reconstruction of DHPR viewed at three different density thresholds. (a) Pink  $2.6\sigma$ , yellow  $1.6\sigma$ , red  $1.25\sigma$  above the mean density displaying a view perpendicular to the EM grid support film and resembling the projection images in Figure 2. Density overlaying the central cavity is indicated by the arrow. (b) Rotation of the view in (a) by  $45^\circ$  ccw around the vertical axis; yellow and red mesh illustrate a finger-like protrusion. (c) Similar view of a second finger protrusion after rotation of (b) by  $180^\circ$  around the vertical axis. (d) At lower thresholding (red) the finger-like protrusion can be seen to form a dome-shaped domain, the broken arrow points to a hole punctuating the dome. The main body of density enclosed by the pink mesh ( $2.4\sigma$ ) is formed by two arches of density, the arrows indicate where the two arches contact each other. (e) View rotated by  $90^\circ$  round the vertical axis with respect to (a). (f) The same view as (e) after imposition of 2-fold symmetry. Scale bar represents 5 nm.

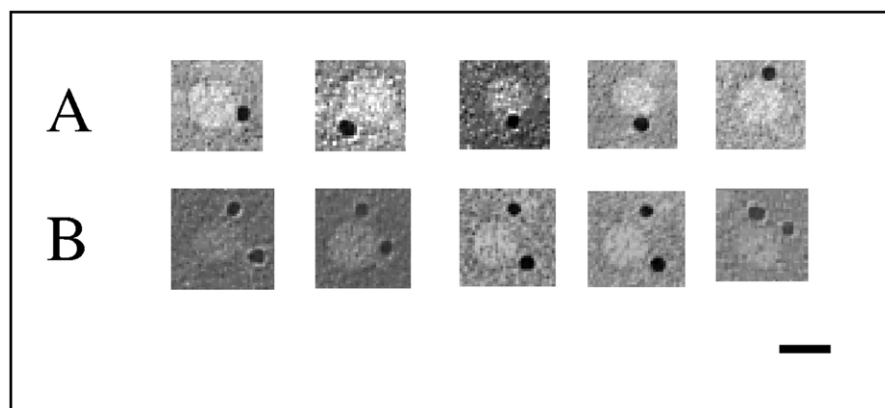


**Figure 4.** Lectin-gold labelled purified DHPR complexes. Row A, Negatively stained (ammonium molybdate) DHPR complexes labelled with a single WGA-gold conjugate (5 nm colloidal gold). Row B, DHPR complexes with two WGA-gold conjugates bound. Scale bar represents 20 nm.

### Lectin-gold labelling of DHPR complexes

Wheat germ agglutinin (WGA) (*Triticum vulgaris*) binds to glycosylated residues and therefore will label the extracellular regions of DHPR.<sup>8</sup> Gold-labelled WGA was therefore incubated with DHPR and then the samples were examined by electron microscopy (EM). For these labelling experiments, ammonium molybdate was found to be the best stain. The majority of DHPR complexes were labelled with a single WGA-gold conjugate bound, (Figure 4, row A). Dual labelled DHPR complexes were also observed (Figure 4, row B). The two WGA-gold particles appeared to be approximately the same distance apart and apparently equidistant from the central axis of the ellipsoidal DHPR complexes, which would be expected if the WGA binding sites were symmetry-related. Intriguingly, the central cavity was not stained by the ammonium molybdate (see Discussion). The dual labelled particles suggest that the 2-fold symmetry axis runs parallel with the plane of the support film, which may be important for differentiating between alternative explanations for the formation of the DHPR dimer, as discussed later.

## Discussion

### Monomer or dimer?

VGCC have been the subject of significant biochemical, physiological and pharmacological study but until recently very little data has been available pertaining to the 3D structure. More success has been obtained with the potassium<sup>49</sup> and sodium voltage-gated channels.<sup>50</sup> Sato and co-workers<sup>50</sup> presented a 3D structure of the voltage-sensitive sodium channel isolated from the eel *Electrophorus electricus*. The polypeptide containing the ion channel (~260 kDa) has the same predicted topology as  $\alpha 1$  DHPR, i.e. four homologous domains that each contain six transmembrane helices,<sup>11</sup> although the skeletal muscle DHPR  $\alpha 1$  subunit is ~70 kDa lower in mass than the sodium channel. The sodium channel is monomeric and has a bell-shape of 13.5 nm in

height, and a square-shaped base of side length 10 nm. Grigorieff and co-workers<sup>49</sup> have recently shown by EM/negative stain that the tetrameric potassium channel is mushroom-shaped, with a thickness of approximately 7 nm as viewed from the cytoplasmic side of the membrane and 11 nm as viewed from the other, with an ~11 nm span perpendicular to the membrane. Each monomer in this channel contains six transmembrane helices giving a similar topology to the sodium and calcium channels. The DHPR 3D volume is large enough (Table 1) to accommodate two sodium channels or two potassium channels. Murata and colleagues<sup>35</sup> have presented projection structures corresponding to particles present in skeletal muscle DHPR preparations. These projections did not display any obvious 2-fold symmetry, and their estimated dimensions of 9 nm  $\times$  10 nm  $\times$  20 nm, approximate to half of the 3D DHPR structure presented here. Thus we suggest that the particles studied by Murata *et al.*, probably correspond to monomeric DHPR.

The 3D structure presented here displays a noticeable 2-fold symmetry, it has a volume that can accommodate at least twice the expected mass of the DHPR polypeptides, and with native PAGE it runs at a mass equivalent to a dimer. Thus we appear to have isolated a dimer of DHPR. It remains to be established whether the DHPR dimer is of functional and physiological significance. Dimerisation occurring after membrane solubilisation by detergent is not unknown, and can be manifested in both head-to-head and a head-to-tail structures. The latter conformation, readily identified as non-physiological, is ruled out by the lectin-gold labelling studies (Figure 4), which appear to show a head-to-head conformation. Thus we conclude that either the DHPR dimer is the true *in vivo* form of DHPR or that detergent solubilisation and purification has resulted in a head-to-head dimer. Cross-linking studies prior to solubilisation might help to clarify this issue in the future. A finding of possible relevance to this issue is that point mutations in the human skeletal  $\alpha 1$  subunit that result in hypokalaemic periodic paralysis give rise to a dominant disease,<sup>51</sup> whereas truncation mutations

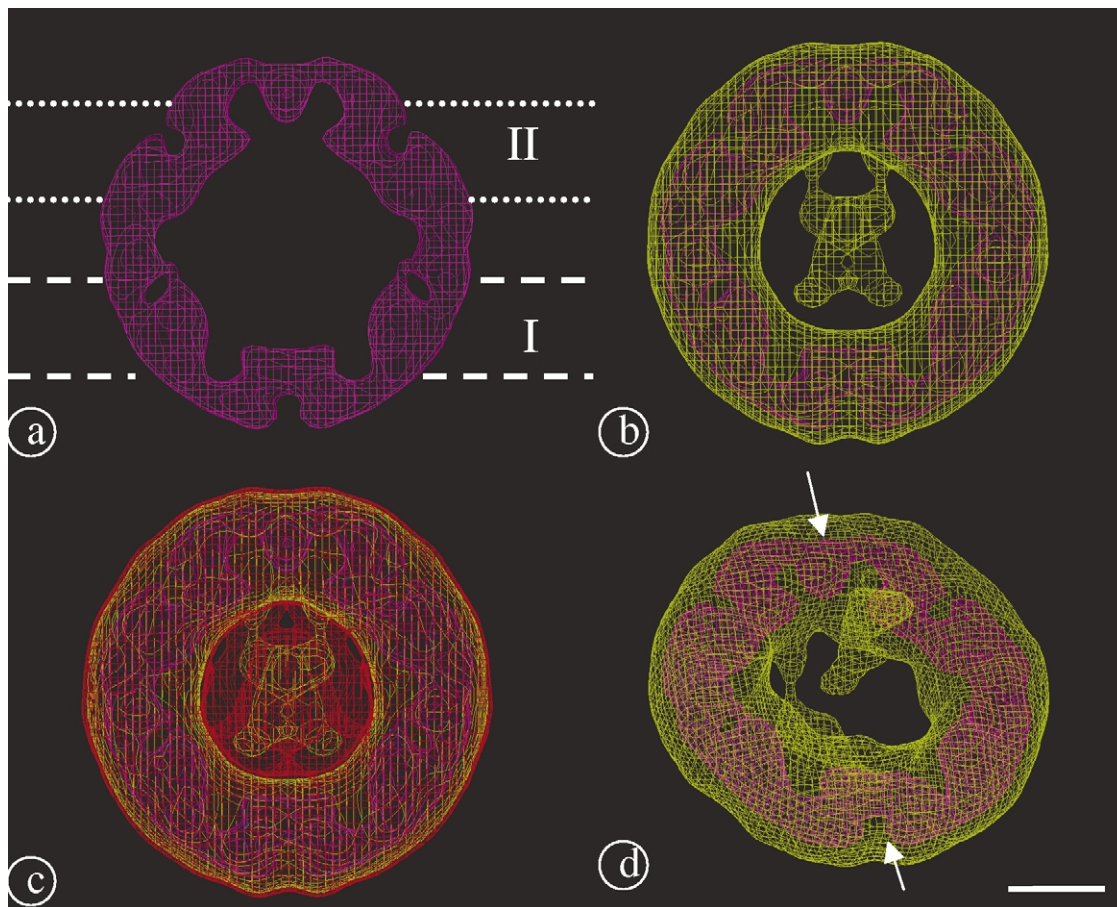


**Figure 5.** 3D structure of the DHPR after 2-fold symmetry has been applied, displayed at decreasing density thresholds ((a)–(c)). (a) The DHPR complex at the highest threshold with two possible locations for the lipid bilayer indicated by broken and dotted lines (I and II, respectively, see Discussion). (d) DHPR complex at the same thresholds as that in (b) but tilted so as to reveal the interior and depth of the central cavity. The arrows in the panel indicate the position of the C2 symmetry axis. Meshing: pink  $2.5\sigma$ , yellow  $1.5\sigma$ , and red  $1.2\sigma$  above the mean density. Scale bar represents 5 nm.

that produce a complete loss of expression of one allele result in a recessive disease.

#### Location of the transmembrane region?

The volumes in [Figure 5](#) show the DHPR dimer after 2-fold symmetry has been applied. [Figure 5\(a\)–\(c\)](#) presents the same view of the volume with different threshold combinations. Two possible locations of the lipid bilayer with respect to the 3D volume are indicated in [Figure 5\(a\)](#), the broken lines representing one position for the transmembrane region in DHPR (I), and the dotted lines another (II). Another possible model (III) could be where one of the finger domains is located on the intracellular side of the membrane and the other on the extracellular side. A DHPR monomer is predicted to contain  $\sim 29$  transmembrane helices and by taking an average of 25 residues for a transmembrane helix, it is clear that only a small (17–25%) proportion of the total mass of each DHPR monomer will actually be located in the lipid bilayer. Moreover, a footprint in the membrane of about 50–100 nm<sup>2</sup> would be

expected for  $\sim 24$  transmembrane helices ( $\alpha 1$  sub-unit), dependent on their packing. These factors would be compatible with models I and II, but not model III, where most of the mass of the protein is in the membrane. In addition model III would not fit with DHPR polypeptide topology predictions, which indicate an asymmetric distribution of protein mass across the t-tubular membrane. [Figure 5\(d\)](#) is displayed at threshold levels comparable to those in (b). In this Figure the symmetrised structure has been rotated so as to reveal the interior and depth of the cavity extending into the finger/dome domains. The arrows indicate the symmetry axis through the volume.

Sections through the 3D volume orientated as shown in [Figure 5\(a\)–\(c\)](#) (surface rendered in SPIDER,  $1\sigma$  above the mean density) taken perpendicular to the 2-fold symmetry axis, displayed at 11 Å intervals, are shown in [Figure 6](#) (direction of slicing running top to bottom). Model I would place the boundaries of the lipid bilayer between slices 4 and 8, corresponding to a thickness of  $\sim 40$ – $50$  Å, whereas in model II the membrane would be placed between slices 4 and 8. It is not

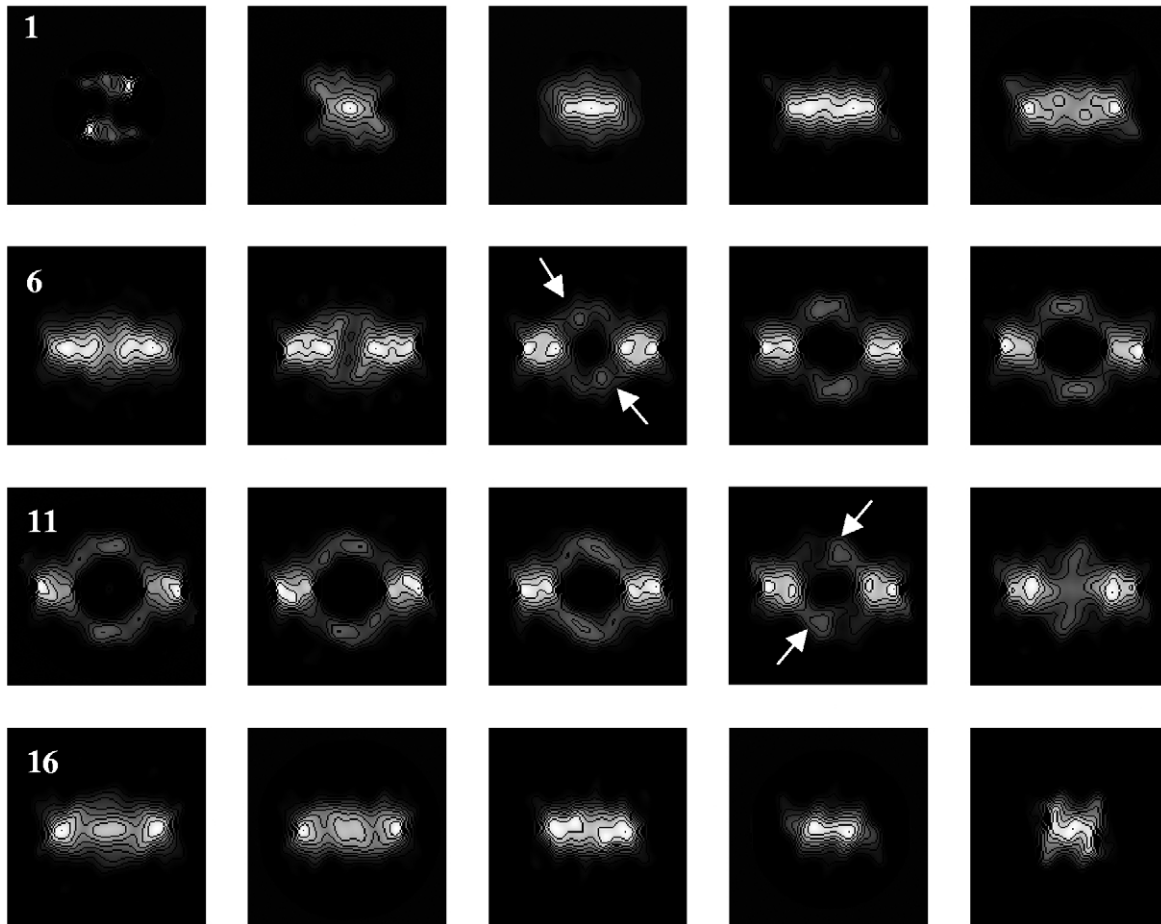


**Figure 6.** Slices at 11 Å intervals through the DHPR 3D structure taken perpendicular to the C2 axis, i.e. as viewed looking down onto the membrane. Slices start from the top through to the bottom through to the top of the structure (as defined in the legend to [Figure 5](#)). Box size, 26 nm × 26 nm.

currently possible to distinguish between models I and II. However, since the majority of the mass of DHPR is on the extracellular side (which is glycosylated), then single particle analysis of the lectin-labelled complexes should in principle offer a route to resolve this problem. The slices also clearly show the finger domains, each one emerging from one side of the complex and interacting with the opposing monomer (indicated by arrows). The contacts between the two DHPR monomers are seen to be most intimate at the top and bottom of the dimeric structure, as also noted in the orientations displayed in [Figure 3](#).

### Interactions with the ryanodine receptor complex

The DHPR complex is a key component of a complex signal-transduction mechanism. In skeletal muscle a number of studies have suggested that the DHPR interacts on its intracellular side with a number of protein components of the triad junction including the RyR<sup>26</sup> and calmodulin.<sup>52</sup> As discussed earlier, in skeletal muscle the direct interaction of the DHPR and the

RyR is believed to form the basis for E–C coupling. The RyR complex (a tetramer) has four large cytoplasmic domains which extend into the gap that separates the t-tubular and jSR membranes as concluded from cryo-EM studies of purified RyR.<sup>53,34</sup> The four globular domains form a square shape with dimensions of 28 nm × 28 nm and 12 nm thick, attached to a central transmembrane region. On each of the four cytoplasmic domains are regions termed the “clamps” and “handles” that form the corners of the square, surrounding a region of low density, and are approximately 19.5 nm apart side to side. A recent study by Samsó *et al.*<sup>54</sup> mapped the four binding sites of imperatoxin A (IpTx<sub>a</sub>) (believed to mimic the cytoplasmic II–III loop of the DHPR α1 subunit) on the RyR to a crevice between the clamp and handle regions. The distance between the four binding sites was determined to be 15 nm. [Figure 7](#) shows how dimeric DHPR complexes could be positioned onto the tetrameric RyR (adapted from Radermacher *et al.*<sup>32</sup>). It is intriguing to note that the dimeric DHPR structure could superimpose on the RyR clamp regions roughly overlaying the IpTx<sub>a</sub> binding domains, and whilst speculative,

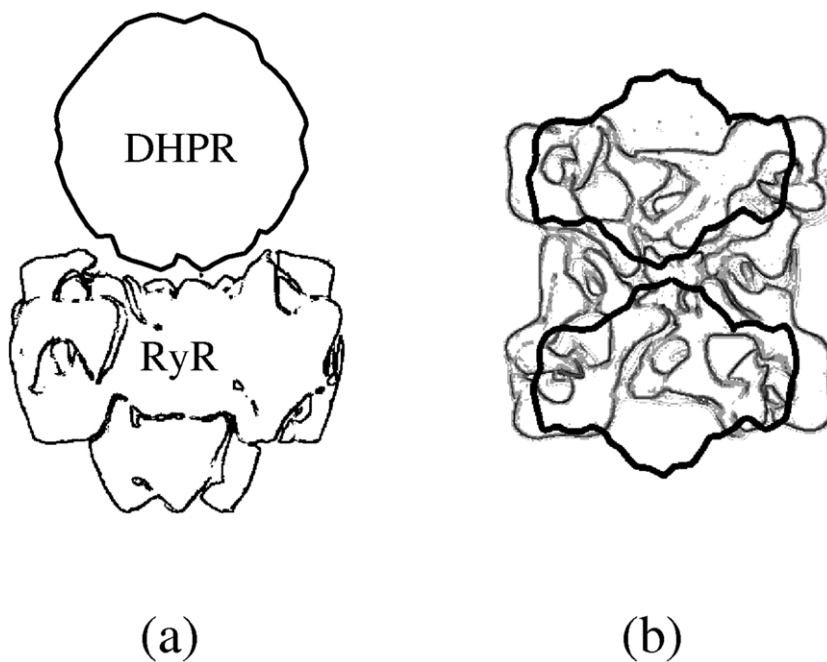


**Figure 7.** Cartoon depicting possible interaction sites of the DHPR complex with the tetrameric RyR complex (adapted from<sup>32</sup>). (a) The complex as viewed parallel with the membrane planes (side view). (b) Superposition of two DHPR dimers on the opposing RyR extracellular face (with respect to the jSR).

this model could now be tested by further structural analyses and cross-linking studies.

### Structure/function relationships

We have presented data from both structural and biochemical studies demonstrating that skeletal muscle DHPR can be isolated as a dimer. An intriguing feature of the dimeric DHPR structure is the large central cavity, which is formed by the two halves of the dimer. If this chamber were to have a function in gating or selectivity, then a physiological role for dimerisation is implicit. Of interest in this respect is the observation of different behaviour of negative stain with respect to the cavity. Whilst the positively charged uranyl ions readily penetrate the cavity, the behaviour of negatively charged molybdate ions is quite different, with little or no staining of the cavity. A larger survey of heavy atom stains is underway.

Future work is now aimed towards the determination of a higher resolution 3D structure of the DHPR, as well as reconstitution of the complexes into lipid bilayers, to further develop and expand upon the data and proposals for the quaternary organisation of the skeletal muscle L-type VGCC presented here.

## Materials and Methods

### Purification

Triads/t-tubules were prepared as described<sup>55</sup> from New Zealand White rabbit skeletal muscle (~2.5–3 kg) and then photoaffinity labelled.<sup>7</sup> DHPR was isolated using a four-step purification based upon the methods described by a number of groups<sup>6–8</sup> i.e. two steps of WGA affinity chromatography, sucrose gradient centri-

fugation, and DEAE-chromatography. All steps were carried out at 4 °C and buffers at each step supplemented with the following protease inhibitors: 0.1 mM phenylmethylsulphonyl fluoride (PMSF), 1 μM pepstatin A, 1 μM *L-trans*-epoxysuccinyl-leucylamide-(4-guanidino)-butane (E64), and 1 mM benzamidine. Triad membranes (2 mg ml<sup>-1</sup>) were solubilised with 1% (w/v) 3-[(cholamidopropyl)dimethyl-ammonio]-1-propanesulphonate (Chaps) (Sigma), 0.5% (w/v) asolecithin (*L*-α-phosphatidylcholine from soyabean, Type II-S, Sigma-Aldrich) at a protein: detergent ratio of 1:5 (w/w). Membranes solubilised with Chaps included the addition of asolecithin in buffers at all stages of the purification.<sup>27</sup> Image processing was carried out on purified DHPR in a final buffer of 20 mM tris(hydroxymethyl)amino-methane (Tris) (pH 7.5), 0.5% (w/v) Chaps, 0.25% (w/v) asolecithin and protease inhibitors.

### Gel electrophoresis

Samples were prepared for denaturing electrophoresis (SDS-PAGE) by incubation of protein with sample buffer (60 mM Tris (pH 6.8), 25% (v/v) glycerol, 2% (w/v) SDS, 14.4 mM 2-mercaptoethanol, 40 mM dithiothreitol (DTT), 1% (w/v) bromophenol blue) at 90 °C for five minutes. 4%–20% gradient gels (Bio-Rad Ltd) were run at 200 V for 45 minutes.

Gels were stained with either 0.1% (w/v) Coomassie blue (in 10% (v/v) methanol, 10% (v/v) glacial acetic acid) or silver stained using a Bio-Rad silver staining kit.

Covalent incorporation of [<sup>3</sup>H]azidopine into triad proteins was detected by liquid scintillation counting of gel slices. Protein bands were visualised by Coomassie staining and then excised from the gels, cut into small pieces and then digested overnight<sup>27</sup> in 0.5 ml of 30% H<sub>2</sub>O<sub>2</sub> at 50 °C. Samples were centrifuged at 13,000g (Eppendorf centrifuge 5415C) and supernatants collected for liquid scintillation counting (Packard 2000CA liquid scintillator).

Native gels with a 4% stacking and 5% separating gel were run at 60 V for five hours (Bio-Rad Mini-Protean II electrophoresis system) at 4 °C. Protein samples in 0.5%

Chaps, 0.25% asolecithin, supplemented with a protease cocktail, as described earlier were combined with an equal volume of sample buffer (60 mM Tris (pH 6.8), 25% glycerol, 1% bromophenol blue). The running buffer was composed of 16.7 mM tricine, 192 mM glycine (pH 8.3) and 0.1% SDS. Molecular mass markers for running on native gels were purchased from Pharmacia.

### Electroelution

Bands were excised from native gels and the protein was electroeluted (five hours) at 4 °C in a BioRad Electro-eluter. Protein was eluted into a 20 mM Tris, 160 mM boric acid (pH 8.4), 0.5 mM EDTA buffer containing 0.5% Chaps, 0.25% asolecithin, and supplemented with protease inhibitors as described above. Eluted protein was examined by EM as described below.

### Immunoblotting

Protein bands from gels were transferred to nitrocellulose using a Biometra Electrophoretic transfer cell. Ponceau S staining (0.2% (w/v) Ponceau S, 3% (v/v) trichloroacetic acid (TCA), 3% (v/v) sulphosalicylic acid) of the nitrocellulose indicated that 90 minutes at 20 V was required for protein transfer. The nitrocellulose was incubated for one hour with the primary antibody (dilution 1:200). An anti-rabbit IgG secondary antibody (Sigma-Aldrich) with an alkaline-phosphatase conjugate was employed for immunodetection. Antisera and affinity purified antibodies raised against anti-beta peptide (Ab2491) and anti-alpha2 peptide (Ab2079) were prepared as described.<sup>15,39</sup> Protein was extracted from nitrocellulose paper by incubating the nitrocellulose in 20% acetonitrile for three hours at 37 °C, after which time the nitrocellulose paper was discarded and the acetonitrile/protein mix lyophilised. The lyophilised protein extract was resuspended in a small volume of SDS sample buffer and the polypeptide composition determined by SDS-PAGE electrophoresis as described above. Silver-stained gels were digitised in transmissive mode (EPSON GT-9600 flatbed scanner) and protein peaks quantified using ImageQuant (v 5.1) after background subtraction.

### Electron microscopy

Samples at 100 µg/ml of protein, were loaded onto carbon-coated grids and negatively stained with 4% (w/v) uranyl acetate as described<sup>56</sup> or 5% (w/v) ammonium molybdate and 1% (w/v) trehalose.<sup>57</sup> Samples were examined in a Philips Tecnai 10 transmission electron microscope at an accelerating voltage of 100 kV under low dose conditions. Electron micrographs were typically taken at 1.7 µm defocus, and were recorded at a calibrated magnification of 43,400 × on Kodak Electron Image film SO-163. Micrographs were digitised on a UMAX PowerLook 3000 scanner with a scan step of 16 µm, corresponding to a pixel size of 3.7 Å at the specimen level.

### Lectin-gold labelling of purified DHPR

Lectin (*T. vulgaris*) conjugated to 5 nm colloidal gold (British Biocell Ltd) was added in excess to the purified DHPR. Samples were incubated for 24 hours (in the presence of protease inhibitors, described above) at 4 °C. Aliquots were taken from the incubation mix, negatively

stained (ammonium molybdate/trehalose) and examined by EM as described above.

### 3D Image processing

The random conical reconstruction method using SPIDER and WEB image processing packages<sup>31</sup> was employed for the calculation of a 3D structure of the DHPR. A total of 35 micrograph pairs (taken at 0° and 50°) of negatively stained (uranyl acetate) DHPR complexes were selected and scanned as described above. Particles were selected from the untilted and tilted micrographs (2405 tilt pairs) and an individual contrast transfer function (CTF) correction was applied to each particle in both data sets based upon its positional co-ordinates. The focus gradient across the tilted micrographs was determined using the software ctfind2.com.<sup>58</sup> The focus gradient parameters for each micrograph were then applied using the SPIDER CTF correction batch files‡.

This file also compensates for the amplitude contrast for negative stain.

The untilted data set was rotationally and translationally aligned using a reference-free alignment algorithm. However, due to the ellipsoidal shape of the DHPR complexes, with axes very similar in length, alignment of the dataset involved initially filtering the particles to 45 Å followed by reference-free alignment. This gave good alignment of the dataset as judged by correspondence analysis and hierarchical ascendant classification. The shifts and rotations used for aligning these heavily filtered particles were then applied to the original dataset, after low pass filtering to 20 Å. Hierarchical clustering, with complete linkage as a merging criterion, was used to separate out the major groups. Only those averages (six classes: 557, 426, 340, 248, 204, 192, and 140 particles, Figure 2, lower panel, row A) with resolutions 25–35 Å were selected for reconstruction of volumes by back projection from the respective tilted particles. Resolution assessment of each major class was determined by plotting the Fourier ring correlation (FRC) between two independent averages. As a measure of resolution for FRC 0.5 was taken as a cut-off.<sup>59</sup>

Each of the six volumes was individually refined six times by optimising the original volume by an angular refinement step (Figure 2, lower panel, row B). In brief, back projections calculated from the initial 3D volume were used to translationally realign the original tilted particles. The realigned particles were then used to create a new volume. The refined volumes from each separate class were then merged after determining the correct Euler angles for combination (Table 1). The groups were merged in order of size, the largest first. The final reconstruction included 1887 images representing 79% of the original tilted dataset. The resolution of this final volume was assessed by the standard method of calculating the FSC<sup>60</sup> between two subvolumes, formed by two half-sets of the selected images, with the resolution limit taken to be at the point where the FSC fell below 0.5.<sup>47</sup> In addition, resolution was assessed by plotting the DPR<sup>48</sup> with 45° used as a cut-off measure.

The 2-fold rotational symmetry of the DHPR complexes isolated here was confirmed by cross-correlation of the unsymmetrised volume with itself after rotation

‡ [http://www.wadsworth.org/spider\\_doc/spider/docs/techs/ctf/ctf.html](http://www.wadsworth.org/spider_doc/spider/docs/techs/ctf/ctf.html)

by 180° around the C2 symmetry axis. Despite the effects of partial staining of one side of the complex, good agreement was found with a value of 0.922. These data are consistent with those from biochemical studies, presented here; indicating that this complex is dimeric.

The approximate protein mass encapsulated at each threshold level used to display the 3D volumes in Figure 3 were determined using the SPIDER commands TH M and FS to calculate the volume fraction above the threshold. This value was then converted to cubic Angstroms. Using a partial specific volume of protein<sup>61</sup> of 0.73 cm<sup>3</sup> g<sup>-1</sup> the molecular mass of the complex at each threshold was calculated.

SPOCK (developed by JA Christopher at Texas A&M) molecular graphics software was used to display 3D volumes using a "chicken wire" effect to illustrate the structure at different thresholding.

## Acknowledgements

This work was funded by the British Heart Foundation via a Basic Science Lectureship Award to Dr A. Kitmitto (BS/97002). The authors acknowledge Dr Richard Collins and Professor Alan Eddy (UMIST) and Dr Anthony Davies (UCL) for useful discussions.

## References

- Hagiwara, S. & Byerly, L. (1981). Calcium channel. *Annu. Rev. Neurosci.* **4**, 69–125.
- Janis, R. A. & Triggle, D. J. (1984). 1,4-Dihydropyridine Ca<sup>2+</sup> channel antagonists and activators—a comparison of binding characteristics with pharmacology. *Drug Dev. Res.* **4**, 257–274.
- Rios, E. & Brum, G. (1987). Involvement of dihydropyridine receptors in excitation contraction coupling in skeletal-muscle. *Nature*, **325**, 717–720.
- Grabner, M., Dirksen, R. T., Suda, N. & Beam, K. G. (1999). The II–III loop of the skeletal muscle dihydropyridine receptor is responsible for the bi-directional coupling with the ryanodine receptor. *J. Biol. Chem.* **274**, 21913–21919.
- Wilkens, C. M., Kasielke, N., Flucher, B. E., Beam, K. G. & Grabner, M. (2001). Excitation–contraction coupling is unaffected by drastic alteration of the sequence surrounding residues L720–L764 of the alpha(1S) II–III loop. *Proc. Natl Acad. Sci. USA*, **98**, 5892–5897.
- Curtis, B. M. & Catterall, W. A. (1984). Purification of the calcium antagonist receptor of the voltage sensitive calcium channel from skeletal muscle transverse tubules. *Biochemistry*, **23**, 2113–2118.
- Sharp, A. H., Imagawa, T., Leung, A. T. & Campbell, K. P. (1987). Identification and characterization of the dihydropyridine-binding subunit of the skeletal-muscle dihydropyridine receptor. *J. Biol. Chem.* **262**, 12309–12315.
- Florio, V., Striessnig, J. & Catterall, W. A. (1992). Purification and reconstitution of skeletal-muscle calcium channels. *Methods Enzymol.* **207**, 529–546.
- Leung, A. T., Imagawa, T. & Campbell, K. P. (1987). Structural characterization of the 1,4-dihydropyridine receptor of the voltage-dependent Ca<sup>2+</sup>-channel from rabbit skeletal-muscle—evidence for 2 distinct high-molecular-weight subunits. *J. Biol. Chem.* **262**, 7943–7946.
- Catterall, W. A. (1988). Structure and function of voltage-sensitive ion channels. *Science*, **242**, 50–61.
- Tanabe, T., Takeshima, H., Mikami, A., Flockerzi, V., Takahashi, H., Kangawa, K. *et al.* (1987). Primary structure of the receptor for calcium-channel blockers from skeletal-muscle. *Nature*, **328**, 313–318.
- Ellis, S. B., Williams, M., Ways, N. R., Brenner, R., Sharp, A. H., Leung, A. T. *et al.* (1988). Sequence and expression of messenger-RNAs encoding the alpha-1 subunit and alpha-2 subunit of DHP-sensitive calcium channel. *Science*, **241**, 1661–1664.
- De Jongh, K. S., Warner, C. & Catterall, W. A. (1990). Subunits of purified calcium channels—alpha-2 and delta are encoded by the same gene. *J. Biol. Chem.* **265**, 14738–14741.
- Jay, S. D., Sharp, A. H., Kahl, S. D., Vedvick, T. S., Harpold, M. M. & Campbell, K. P. (1991). Structural characterization of the dihydropyridine-sensitive calcium-channel alpha-2-subunit and the associated delta-peptides. *J. Biol. Chem.* **266**, 3287–3293.
- Brickley, K., Campbell, V., Berrow, N., Leach, R., Norman, R. I., Wray, D. *et al.* (1995). Use Of site-directed antibodies to probe the topography of the alpha(2) subunit of voltage-gated Ca<sup>2+</sup> channels. *FEBS Letters*, **364**, 129–133.
- Gurnett, C. A., De Waard, M. & Campbell, K. P. (1996). Dual function of the voltage-dependent Ca<sup>2+</sup> channel alpha(2)delta subunit in current stimulation and subunit interaction. *Neuron*, **16**, 431–440.
- Walker, D. & De Waard, M. (1998). Subunit interaction sites in voltage-dependent Ca<sup>2+</sup> channels: role in channel function. *Trends Neurosci.* **21**, 148–154.
- Jay, S. D., Ellis, S. B., McCue, A. F., Willimas, M. E., Vedvick, T. S., Harpold, M. M. & Campbell, K. P. (1990). Primary structure of the gamma-subunit of the DHP-sensitive calcium-channel from skeletal muscle. *Science*, **248**, 490–492.
- Hofmann, F., Biel, M. & Flockerzi, V. (1994). Molecular-basis for Ca<sup>2+</sup> channel diversity. *Annu. Rev. Neurosci.* **17**, 399–418.
- DeWaard, M., Scott, V. E. S., Pragnell, M. & Campbell, K. P. (1996). Identification of critical amino acids involved in alpha(1)–beta interaction in voltage-dependent Ca<sup>2+</sup> channels. *FEBS Letters*, **380**, 272–276.
- Brice, N. L., Berrow, N. S., Campbell, V., Page, K. M., Brickley, K., Tedder, I. & Dolphin, A. C. (1997). Importance of the different beta subunits in the membrane expression of the alpha 1A and alpha 2 calcium channel subunits: studies using a depolarization-sensitive alpha 1A antibody. *Eur. J. Neurosci.* **9**, 749–759.
- Gurnett, C. A., Felix, R. & Campbell, K. P. (1997). Extracellular interaction of the voltage-dependent Ca<sup>2+</sup> channel alpha(2)delta and alpha(1) subunits. *J. Biol. Chem.* **272**, 18508–18512.
- Gao, T., Chien, A. J. & Hosey, M. M. (1999). Complexes of the alpha(1C) and beta subunits generate the necessary signal for membrane targeting of class C L-type calcium channels. *J. Biol. Chem.* **274**, 2137–2144.
- Franzini-Armstrong, C. (1984). Freeze-fracture of frog slow tonic fibres:structure of surface and internal membranes. *Tissue Cell*, **16**, 146–166.
- Block, B. A., Imagawa, T., Leung, A., Campbell, P. & Franzini-Armstrong, C. (1988). Structural evidence

- for direct interaction between the molecular-components of the transverse tubule sarcoplasmic-reticulum junction in skeletal-muscle. *J. Cell Biol.* **107**, 2587–2600.
26. Franzini-Armstrong, C. & Jorgenson, A. O. (1994). Structure and development of E–C coupling units in skeletal muscle. *Annu. Rev. Physiol.* **56**, 509–534.
27. Leung, A. T., Imagawa, T., Block, B., Franzini-Armstrong, C. & Campbell, K. P. (1988). Biochemical and ultrastructural characterization of the 1,4-dihydropyridine receptor from rabbit skeletal-muscle—evidence for a 52,000 Da subunit. *J. Biol. Chem.* **263**, 994–1001.
28. van Heel, M., Gowen, B., Matadeen, R., Orlova, E. V., Finn, R., Pape, T. *et al.* (2000). Single-particle electron cryo-microscopy: towards atomic resolution. *Quart. Rev. Biophys.* **33**, 307–369.
29. Radermacher, M. (1988). 3-Dimensional reconstruction of single particles from random and nonrandom tilt series. *J. Electron Microsc. Tech.* **9**, 359–394.
30. Schatz, M., Orlova, E. V., Dube, P., Jager, J. & van Heel, M. (1995). Structure of lumbricus-terrestris hemoglobin at 30 Å resolution determined using angular reconstitution. *J. Struct. Biol.* **114**, 28–40.
31. Frank, J., Radermacher, M., Penczek, P., Zhu, J., Li, Y. H., Ladjadj, M. & Leith, J. (1996). SPIDER and WEB: processing and visualization of images in 3D electron microscopy and related fields. *J. Struct. Biol.* **116**, 190–199.
32. Radermacher, M., Rao, V., Grassucci, R., Frank, J., Timerman, A. P., Fleischer, S. & Wagenknecht, T. (1994). Cryoelectron microscopy and 3-dimensional reconstruction of the calcium-release channel ryanodine receptor from skeletal-muscle. *J. Cell Biol.* **127**, 411–423.
33. Saibil, H. (2000). Molecular chaperones: containers and surfaces for folding, stabilising or unfolding. *Curr. Opin. Struct. Biol.* **10**, 251–258.
34. Chiu, W. & Schmid, M. F. (1997). Pushing back the limits of electron cryomicroscopy. *Nature Struct. Biol.* **4**, 331–333.
35. Murata, K., Odahara, N., Kuniyasu, A., Sato, Y., Nakayama, H. & Nagayama, K. (2001). Asymmetric arrangement of auxiliary subunits of skeletal muscle voltage-gated L-type Ca<sup>2+</sup> channel. *Biochem. Biophys. Res. Commun.* **282**, 284–291.
36. Harris, J. R. & Horne, R. W. (1994). Negative staining: a brief assessment of current technical benefits, limitations and future possibilities. *Micron*, **25**, 5–13.
37. Holzenburg, A., Flint, T. D., Shepherd, F. H. & Ford, R. C. (1996). Photosystem II: mapping the locations of the oxygen evolution-enhancing subunits by electron microscopy. *Micron*, **27**, 121–127.
38. Rosenberg, M. F., Velarde, G., Ford, R. C., Martin, C., Berridge, G., Kerr, I. D. *et al.* (2001). Repacking of the transmembrane domains of P-glycoprotein during the transport ATPase cycle. *EMBO J.* **20**, 5615–5625.
39. Berrow, N., Tedder, I., Page, K., Brice, N., Amos, B. & Dolphin, A. C. (1995). Properties of alpha(1a) calcium-channel currents is expressed in the Cos-7 cell-line. *J. Physiol. (Lond.)*, **489P**, P52–P53.
40. Flockerzi, V., Oeken, H.-J. & Hofmann, F. (1986). Purification of a functional receptor for calcium-channel blockers from rabbit skeletal-muscle microsomes. *Eur. J. Biochem.* **161**, 217–224.
41. Tischendorf, G. W., Zeichhardt, H. & Stöffler, G. (1974). Determination of the location of proteins L14, L17, L18, L19, L22, and L23 on the surface of the 50 S ribosomal subunit of *Escherichia coli* by immunoelectron microscopy. *Mol. Gen. Genet.* **134**, 187–204.
42. Venien-Bryan, C., Lowe, E. M., Boisset, N., Traxler, K. W., Johnson, L. N. & Carlson, G. M. (2002). Three-dimensional structure of phosphorylase kinase at 22 Å resolution and its complex with glycogen phosphorylase b. *Structure*, **10**, 33–41.
43. Mayanagi, K., Miyata, T., Oyama, T., Ishino, T. & Morikawa, K. (2001). Three-dimensional electron microscopy of the clamp loader small subunit from *Pyrococcus furiosus*. *J. Struct. Biol.* **134**, 35–45.
44. Penczek, P., Radermacher, M. & Frank, J. (1992). Three-dimensional reconstruction of single particles embedded in ice. *Ultramicroscopy*, **40**, 33–53.
45. Frank, J. (1982). New methods for averaging non-periodic objects and distorted crystals in biologic electron microscopy. *Optik*, **63**, 67–89.
46. Boekema, E. J. (1991). Negative staining of integral membrane proteins. *Micron Microsc. Acta*, **22**, 361–369.
47. Böttcher, B., Wynne, S. A. & Crowther, R. A. (1997). Determination of the fold of the core protein of hepatitis B virus by electron microscopy. *Nature*, **386**, 88–91.
48. Frank, J., Verschoor, A. & Boublik, M. (1981). Computer averaging of electron micrographs of 40 S ribosomal subunits. *Science*, **214**, 1353–1355.
49. Sokolova, O., Kolmakova-Partensky, L. & Grigorieff, N. (2001). Three-dimensional structure of a voltage-gated potassium channel at 2.5 nm resolution. *Structure*, **9**, 215–220.
50. Sato, C., Ueno, Y., Asai, K., Takahashi, K., Sato, M., Engel, A. & Fujiyoshi, Y. (2001). The voltage-sensitive sodium channel is a bell-shaped molecule with several cavities. *Nature*, **409**, 1047–1051.
51. Lapie, P., Lory, P. & Fontaine, B. (1997). Hypokalemic periodic paralysis: an autosomal dominant muscle disorder caused by mutations in a voltage-gated calcium channel. *Neuromusc. Disord.* **7**, 234–240.
52. Zühlke, R. D., Pitt, G. S., Deisseroth, K., Tsien, R. W. & Reuter, H. (1999). Calmodulin supports both inactivation and facilitation of L-type calcium channels. *Nature*, **399**, 159–162.
53. Serysheva, I. I., Orlova, E. V., Chiu, W., Sherman, M. B., Hamilton, S. L. & van Heel, M. (1995). Electron cryomicroscopy and angular reconstitution used to visualize the skeletal-muscle calcium-release channel. *Struct. Biol.* **2**, 18–24.
54. Samsó, M., Trujillo, R., Gurrola, G. B., Valdivia, H. H. & Wagenknecht, T. (1999). Three-dimensional location of the imperatoxin A binding site on the ryanodine receptor. *J. Cell Biol.* **146**, 493–499.
55. Glossman, H. & Ferry, D. R. (1983). Solubilization and partial-purification of putative calcium channels labeled with nimodipine-H-3. *Naunyn-Schmiedeberg Arch. Pharmacol.* **323**, 279–291.
56. Holzenberg, A., Shepherd, F. H. & Ford, R. C. (1994). Localization of the oxygen-evolving complex of photosystem-II by Fourier difference analysis. *Micron*, **25**, 447–451.
57. Harris, J. R., Hoeger, U. & Adrian, M. (2001). Transmission electron microscopical studies on some haemolymph proteins from the marine polychaete *Nereis virens*. *Micron*, **32**, 599–613.
58. Crowther, R. A., Henderson, R. & Smith, J. M. (1996). MRC image processing programs. *J. Struct. Biol.* **116**, 9–16.

59. vanHeel, M. (1987). Similarity measures between images. *Ultramicroscopy*, **21**, 95–99.
60. Harauz, G. & van Heel, M. (1986). Exact filters for general geometry three-dimensional reconstruction. *Optik*, **73**, 146–156.
61. Holzenburg, A., Bewley, M. C., Wilson, F. H., Nicholson, W. V. & Ford, R. C. (1993). Three dimensional structure of photosystem II. *Nature*, **363**, 470–472.

*Edited by I. B. Holland*

*(Received 7 May 2002; received in revised form 9 August 2002; accepted 9 August 2002)*